Chin. J. Astron. Astrophys. Vol. 6 (2006), No. 5, 597–607
(*http://www.chjaa.org*)

Chinese Journal of
Astronomy and
Astrophysics

Spectral Analysis and Atmospheric Models of Microflares *

Cheng Fang[1], Yu-Hua Tang[1] and Zhi Xu[1,2]

[1] Department of Astronomy, Nanjing University, Nanjing 210093; *fangc@nju.edu.cn*
[2] National Astronomical Observatories / Yunnan Observatory, Chinese Academy of Sciences, Kunming 650011

Received 2006 February 7; accepted 2006 February 20

Abstract By use of the high-resolution spectral data obtained with THEMIS on 2002 September 5, the spectra and characteristics of five well-observed microflares have been analyzed. Our results indicate that some of them are located near the longitudinal magnetic polarity inversion lines. All the microflares are accompanied by mass motions. The most obvious characteristic of the Hα microflare spectra is the emission at the center of both Hα and CaII 8542 Å lines. For the first time both thermal and non-thermal semi-empirical atmospheric models for the conspicuous and faint microflares are computed. In computing the non-thermal models, we assume that the electron beam resulting from magnetic reconnection is produced in the chromosphere, because it requires lower energies for the injected particles. It is found there is obvious heating in the low chromosphere. The temperature enhancement is about 1000–2200 K in the thermal models. If the non-thermal effects are included, then the required temperature increase can be reduced by 100–150 K. These imply that the Hα microflares can probably be produced by magnetic reconnection in the solar lower atmosphere. The radiative and kinetic energies of the Hα microflares are estimated and the total energy is found to be $10^{27} - 4\times10^{28}$ erg.

Key words: Sun: Microflares – Sun: spectrum – Sun: semi-empirical modelling

1 INTRODUCTION

It is well known that microflares (MFs), or subflares, as they are often called, are small short-lived brightenings, which have been observed and studied for decades (e.g. Svestka 1976; Tandberg-Hanssen & Emslie 1988). In the past, some authors have also called them bright points or miniflares, etc. The size of MFs is from several arcsec to about $20''$, their typical lifetime is 10–30 minutes and their energy has been estimated to be $10^{26} - 10^{29}$ erg (Shimizu et al. 2002).

The most obvious characteristic of MFs' visible spectra is the weak emission at the center of chromospheric lines. The Hα line is thus the most common studied one, and the area on the Hα filtergrams is an important criterion for MFs (subflares). However, soft X-ray (Golub et al. 1974, 1977), hard X-ray (Lin et al. 1984), EUV (Porter et al. 1984; Emslie & Noyes 1978), as well as microwave (e.g. Gary et al. 1988) emissions have also been observed in some MFs. Recently, RHESSI has successively obtained the first hard X-ray image of MFs (Krucker et al. 2002; Benz & Grigis 2002). Some of the observations implied that the emissions in different wavelengths are coincident . For instance, by use of SMM data, Porter et al. (1987) found that the long lived UV brightenings in the C IV line were coincident with soft X-ray MFs. Berghmans et al. (2001) compared the data of Yohkoh/SXT, SOHO/EIT and TRACE, and found that the strongest EUV brightenings were counterparts of soft X-ray MFs. Liu et al. (2004) compared BBSO/Hα, RHISSI images in 3 to 15 keV and GOES data for 12 MFs, and found all of them are seen in soft X-ray, hard X-ray and Hα

* Supported by the National Natural Science Foundation of China.

wavelengths. Qiu et al. (2004) found that about 40% of the MFs exhibit hard X-ray emission at over 10 keV and microwave emission at around 10 GHz. However, it is obvious that we should not always expect to see simultaneous emissions in the different wavelengths, for much depends on the heating condition of the particular MF. However, for MFs with emission at the center of Hα line, which may be called Hα MFs, the heating region should be at least in the solar chromosphere.

Mass motion has been observed at or near the location of MFs. Shimizu et al. (2002) found that chromospheric ejections are observed in some MFs, and X-ray jets were also observed in some MFs. It was also found that some MFs are located close to, or across magnetic polarity inversion lines (Porter et al. 1987; Wang et al. 1999; Shimizu et al. 2002; Liu et al. 2004). Non-thermal properties of MFs are well explored in the microwave (e.g. Gary & Zirin 1988; White et al. 1995; Nindos et al. 1999) and hard X-ray emissions (e.g., Nitta 1997; Liu et al. 2004; Qiu et al. 2004). Some MFs are even associated with type III bursts (e.g. Liu et al. 2004), which is a clear signature of the presence of non-thermal electrons. Moreover, it was also found that in many cases emerging flux occurs about 5–30 minutes before the MFs (e.g. Tang et al. 2000; Shimizu et al. 2002).

All these observations imply that magnetic reconnection in the lower solar atmosphere could be a plausible mechanism for triggering MFs (Tandberg-Hanssen & Emslie 1988; Liu et al. 2004). Chen et al. (2001) made a 2D numerical MHD simulation, and found that magnetic reconnection in the lower solar atmosphere could explain some characteristics of MFs, such as the temperature enhancement and lifetime, etc.

To well explore the nature of MFs, it is very important to know their atmospheric structure. However, spectral observations with high spatial resolution that is essential for constructing accurate atmospheric model of MFs have been few up to now. In this paper we use high-resolution spectral data of Hα, CaII 8542 Å, and FeI 6302.5 Å lines obtained with the French-Italian 90 cm vacuum telescope, THEMIS, on 2002 September 5. The characteristics of five well-observed Hα MFs have been analyzed. For two typical MFs, representing bright and faint events, we have computed semi-empirical atmospheric models, with or without considering non-thermal excitation and ionization effects. We have also studied the relationship between MFs and magnetic and velocity fields.

Features of the THEMIS observations are described in Section 2. In Section 3 the characteristics of the MFs are analyzed, including their relationship with the magnetic and velocity fields. Semi-empirical atmospheric models for the two MFs are given in Section 4. A discussion and conclusions are given in Section 5.

2 SPECTROPOLARIMETRIC OBSERVATIONS OF MICROFLARES

The active region 10096 (S16E09) was observed on 2002 September 5 from 08:01 UT to 12:07 UT with the French-Italian solar telescope, THEMIS, in the MTR multi-line spectropolarimetric mode (*www.themis.iac.es*). In this mode two beams with orthogonal polarization exiting the analyzer are directed into a single camera. The top part of the camera receives sequentially I+Q, I+U, I+V and I-V, while the bottom part records I-Q, I-U, I-V and I+V. Three cameras record simultaneously the Stokes parameters for Hα, CaII 8542 Å and FeI 6302.5 Å lines.

The active region was scanned several times in 80 steps separated by $1''$ in space. The spatial sampling along the slit is $0.42''$/pixel. The spectral sampling is 26.1 mÅ for Hα, 36.3 mÅ for CaII 8542, and 22.4 mÅ for FeI 6302.5 Å. The seeing condition is better than $1''$, but the scanning limited the spatial resolution to about $2''$ for all 2D maps.

After dark current and flat-field were corrected, the Muller matrix was used to demodulate the Stokes parameters. To remove induced cross-talk and improve the seeing smearing, we sum the top and the bottom spectra. To do so, the two spectra are well aligned in the slit direction (y direction). By use of the Stokes V profiles of the FeI 6302.5 Å line, the longitudinal magnetic field can be derived. However, due to the low S/N ratio, the transverse magnetic field cannot be convincingly deduced from the Stokes parameters Q and U. The 2D velocity fields were obtained using the bisector method with the Hα line profiles. Owing to the fact that all lines were observed simultaneously, the 2D intensity, velocity and magnetic fields are exactly coaligned.

3 CHARACTERISTICS OF THE MICROFLARES

3.1 Well-observed Microflares

By checking the 2D spectra, we found five well-observed MFs during the observations. Table 1 lists some characteristics of the MFs, including the scan time, location, intensity, duration, size and accompanied mass ejection. In the column showing the location the (x, y) coordinates of the MF are in pixels, with x along the scan direction, and y along the slit direction and the interval between two pixels $0.42''$. The relationship of the MF with the longitudinal magnetic field is also given: NN means that the MF is near the magnetic polarity inversion lines (less than $6''$). According to the excess Hα peak intensity ΔI (MF intensity with the quite-Sun background subtracted), the MFs are classified into bright and faint ones, according as $\Delta I \geq 10$ or < 10, in units of erg s^{-1} cm^{-2} sr^{-1} Å^{-1}. The duration is estimated by the scanning times during which the MF appears. Owing to the low cadence of the scanning, the estimated durations of the MFs may be lower limits. If the MF appears only in one scan then the duration should be less than the period between the previous and following scan, which is an upper limit for the lifetime of the MF. The average sizes are estimated by counting how many pixels on the spectra along the slit and how many steps along the scan direction that the MF can be still identified.

Table 1 Characteristics of the Observed MFs

No.	Time (UT)	Location (x, y)	Intensity	Duration (min)	Size (arcsec)	Mass ejection
1	0812	93, 65 NN	bright	$\geq$40	7	yes
2	0812	124, 48	faint	$\geq$30	5	yes
3	0947	98, 77 NN	faint	$<$20	4	yes
4	0959	121, 68	bright	/	9	yes
5	1149	17, 11 NN	bright	/	5	yes

From Table 1 it can be seen that the sizes of the MFs are about $4''$–$9''$, and generally the fainter MFs are smaller than the brighter MFs. Moreover, three MFs are located near the magnetic polarity inversion lines, and all the MFs are accompanied by downward and/or upward flows, although some of the ejections are not strong.

3.2 Spectral Characteristics

Figures 1–2 show the Hα and CaII 8542 spectral profiles for one bright (No.1) and one faint (No.3) MF, respectively. The line intensities of the MFs with the quiet-Sun background subtracted (MF-Q) are also shown. It is seen that all the MF-Q profiles show excess emission around the line center. It implies that compared to the quiet-Sun region, the heating of the Hα MFs is significant in the chromosphere. This can be clearly seen in the semi-empirical atmospheric models which will be presented in Section 4.

3.3 Locations of the MFs on 2D Magnetic and Velocity Maps

Figure 3 gives the locations of the four MFs on the 2D Hα images at 08:12 UT (left) and 09:59 UT (right). The crosses mark the positions of the MFs. We do not give the position of the No.5 MF, because it was observed at a much later time when the image had changed. Also shown are longitudinal magnetic field contours at levels –800, –300, –50, –5, 4, 40, 200 and 500 G, in green (purple) for negative (positive) polarity. Figure 3 shows clearly that three of the MFs appear close to the magnetic polarity inversion lines. Moreover, there is a two-ribbon brightening in the lower-left part of this figure. It is an interesting two-ribbon small flare, which we will analyze in another paper. Figure 4 shows the velocity distribution at 08:12 UT and 09:59 UT, and the size of the Doppler velocity is color-coded. Owing to the rapid changes of the velocity field, only the MFs appearing around the given times, i.e., the two MFs (Nos. 1 and 2) around 08:12 UT and the two MFs (Nos. 3 and 4) at or near 09:59 UT, are marked by crosses. It can be seen from the figure that the MFs are closely related to mass motions, and Nos. 3 and 4 MFs both even have upward and downward motions of different velocities on either side. It implies that the MFs are accompanied by plasma ejections, which provide evidence for magnetic reconnection.

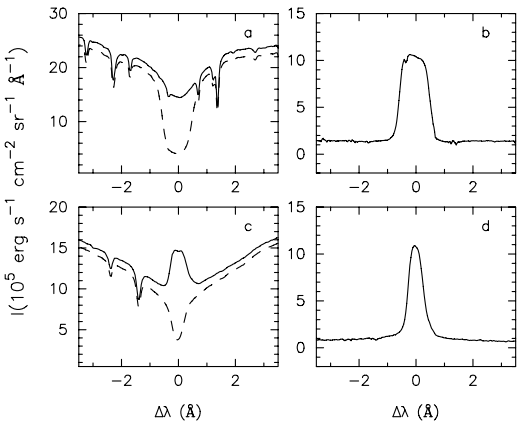

Fig. 1 Hα and CaII 8542 Å line profiles of a bright MF (No.1). Panel (a) shows the Hα profile (solid) and the quite-Sun background (dashed), and Panel (b) shows the "net" profile (Hα - Q); Panels (c) and (d) do the same for the CaII 8542 Å line.

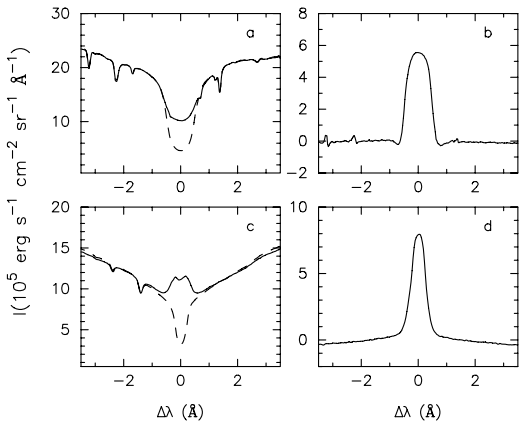

Fig. 2 Same as Fig. 1, but for a faint MF (No.3).

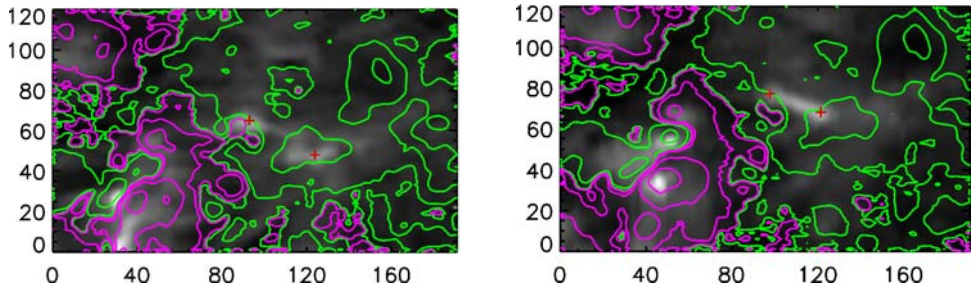

Fig. 3 Locations for two well-observed MFs (Nos. 1 and 2) on the 2D images of the Hα center at 08:12 UT (left), and for two other MFs (Nos. 3 and 4) at 09:59 UT (right). The contour levels of the longitudinal magnetic field are –800, –300, –50, –5, 4, 40, 200 and 500 G, green for negative polarity, purple for positive polarity.

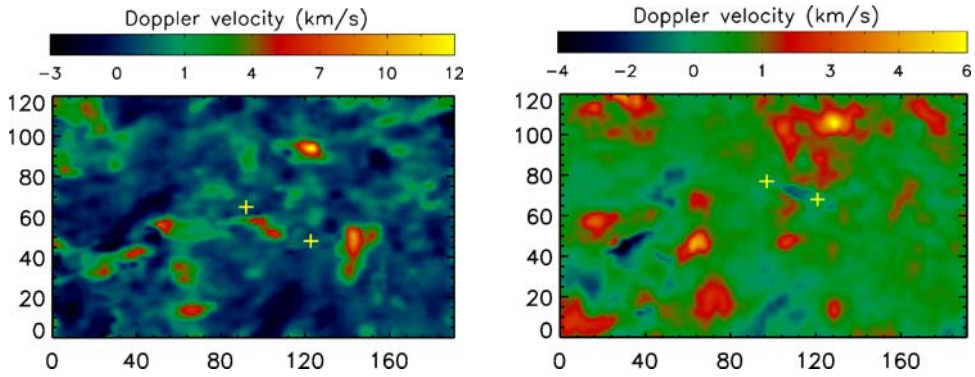

Fig. 4 Color-coded velocity distributions at 08:12 UT (left) and 09:59 UT (right). Yellow crosses mark the locations of MFs (Nos. 1 and 2) in the left panel and of MFs (Nos. 3 and 4) in the right panel.

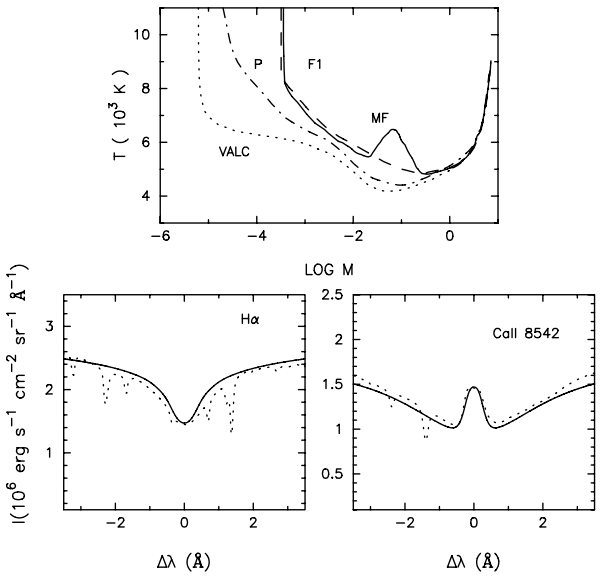

Fig. 5 Upper panel shows the temperature distributions in the thermal semi-empirical model for the bright MF (No.1) (solid line), compared to those for the plage model (P) (dotted-dashed line) given by Fang et al. (2001), the quiet-Sun model (VALC) (dotted line) given by Vernazza et al. (1981), and the flare model F1 (dashed line) given by Machado et al. (1980). The lower panels compare the computed line profiles (solid lines) with the observed ones (dotted lines) for Hα (lower left penal) and CaII 8542 Å (lower right penal). A Gaussian macroturbulence velocity of 10 km s^{-1} for the Hα line and 6 km s^{-1} for the CaII line is adopted to convolve the computed line profiles.

4 SEMI-EMPIRICAL ATMOSPHERIC MODELS OF THE MFS

4.1 Computation of Semi-empirical Atmospheric Models

By the use of both Hα and CaII 8542 Å line profiles, semi-empirical atmospheric models of the MFs can now be computed with less ambiguity. The method of the non-LTE computation is similar to that given by Fang et al. (1993), that is, we used two atomic models, one a four-level plus continuum for hydrogen, one a five-level plus continuum for calcium. The statistical equilibrium equation and the transfer equation, coupled with the hydrostatic equilibrium and the particle conservation equations, were solved iteratively. To ensure sufficient convergence, more than 12000 iterations were taken, until the relative difference in the mean intensity between the last two iterations is within 10^{-5} for hydrogen and 10^{-8} for calcium.

The thermal semi-empirical models for the two typical MFs (Nos. 1 and 3) are computed, which can well reproduce both the observed Hα and CaII 8542 Å line profiles. Figures 5–6 give the thermal semi-empirical atmospheric models and both the observed and computed line profiles of the two MFs. For comparison, the temperature distributions of the semi-empirical models for a plage (P) given by Fang et al. (2001), for a typical faint flare (F1) given by Machado et al. (1980), and for the quiet-Sun model (VALC) given by Vernazza et al. (1981), are also shown in these figures. It can be seen from Figures 5–6 that a common characteristic of the thermal models is the obvious heating in the chromosphere. The temperature enhancement is about 1000–2200 K. The higher value corresponds to the temperature bump up in the low-chromosphere. The temperature increase is higher for the bright MF than that for the faint one.

However, since magnetic reconnection is probably the mechanism for flares of all sizes (Parker 2001), including MFs, energetic particles should be produced during the reconnection. Considering that electron beam bombardment is more effective than proton beam bombardment, as indicated by Fang et al. (1993) and Hénoux et al. (1995), we also compute the non-thermal semi-empirical models with the excitation and ionization by electron beam bombardment included, assuming that the reconnection site is in the chromosphere. The reason is that the heating resulted from magnetic reconnection is significant in the low-chromosphere.

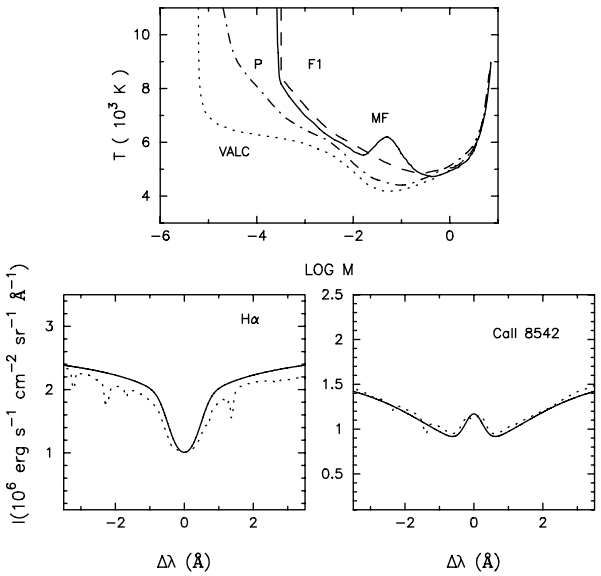

Fig. 6 Same as Fig. 5, but for the faint MF (No. 3). The same Gaussian macro-turbulence velocity is adopted to convolve the computed line profiles.

According to the magnetic reconnection scenario, during the magnetic reconnection oppositely-oriented electron beams are ejected from the reconnection site, so in our computation both upward and downward bombardments are considered.

Following the theory given by Fang et al. (1993) and Hénoux et al. (1995), for an electron beam bombardment, the non-thermal collisional excitation and ionization rates of hydrogen from its ground level 1 to the higher levels 2–4 and the continuum c, can be taken, to a good approximation, as

$$C_{12} \simeq 2.94\times10^{10}\frac{1}{n_1}\frac{dE^{\rm H}}{dt}, \quad \text{and} \quad C_{13} \simeq 5.35\times10^{9}\frac{1}{n_1}\frac{dE^{\rm H}}{dt},$$
$$C_{14} \simeq 1.91\times10^{9}\frac{1}{n_1}\frac{dE^{\rm H}}{dt}, \quad \text{and} \quad C_{1c} \simeq 1.73\times10^{10}\frac{1}{n_1}\frac{dE^{\rm H}}{dt}. \tag{1}$$

The non-thermal collisional excitation and ionization rates of CaII can be expressed as

$$C_{14} \simeq 2.38\times10^{10}\frac{1}{n_1}\frac{dE^{\rm H}}{dt},$$
$$C_{15} \simeq 4.25\times10^{10}\frac{1}{n_1}\frac{dE^{\rm H}}{dt},$$
$$C_{1c} \simeq 4.69\times10^{10}\frac{1}{n_1}\frac{dE^{\rm H}}{dt}, \tag{2}$$

where n_1 is the ground level population. The excitation and ionization from the higher levels are negligible. Here $dE^{\rm H}/dt$ is the rate of energy deposition due to the excitation and ionization of hydrogen by an electron beam. Neglecting the return current effects in a dense atmosphere, the energy deposit rate is given by Emslie (1978) and Chambe & Hénoux (1979) as

$$\frac{dE^{\rm H}}{dt} = \frac{1}{2}(1-x)n_{\rm H}\Lambda'\frac{K\,\mathcal{F}_1}{E_1^2}\Big(\frac{N}{N_1}\Big)^{-\frac{\delta}{2}}(\delta-2)\int_0^{u_1}\frac{u^{\frac{\delta}{2}-1}du}{(1-u)^{\frac{2+\beta}{4+\beta}}}, \tag{3}$$

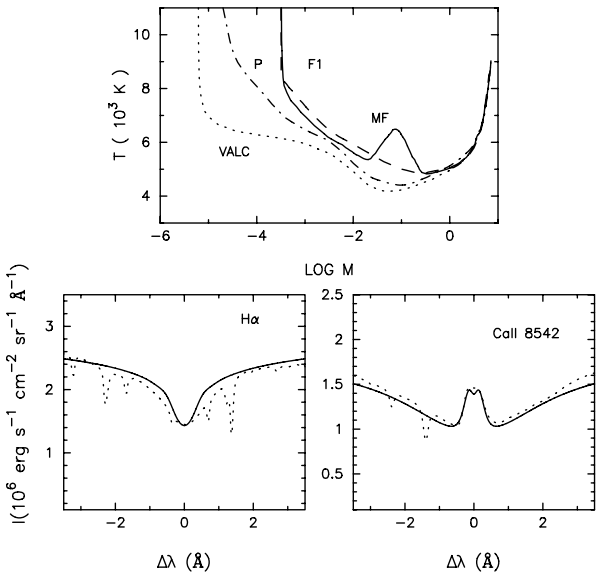

Fig. 7 Same as Fig.6, but for the non-thermal semi-empirical model of the bright MF (No. 1). The electron beam flux $\mathcal{F}_1 = 1 \times 10^{10}$ erg cm^{-2} s^{-1}, the low cut-off energy $E_1 = 20$ keV, and the power index $\delta = 5$.

where x is the degree of ionization. The particle flux is supposed to be proportional to $E^{-\delta}$, with a low cut-off energy E_1. $\mathcal{F}_1$ is the total energy input flux above E_1. The meaning of other physical quantities can be found in the original references.

We solve iteratively the rate equation that includes the non-thermal collisional excitation and ionization rates, coupled with the transfer equation, the hydrostatic equilibrium and the particle conservation equations. For an assumed electron beam flux and power index, we compute the non-thermal semi-empirical models. The computed model for the bright MF (No. 1) and the corresponding computed line profiles are given in Figure 7. In this case we took an electron beam flux of $\mathcal{F}_1$ = 1 $\times 10^{10}$ erg cm^{-2} s^{-1}, a power index of δ = 5, and the low cut-off energy $E_1 = 20$ keV. From Figures 5–7 it can be seen that both the thermal and non-thermal theoretical line profiles can well reproduce the observed profiles. The two models have the common feature of a temperature bump in the low-chromosphere. The temperature enhancement is about 2200 K above the quite-Sun VALC model. This gives additional evidence for our assumption that the reconnection site is in the low-chromosphere. However, for the case with non-thermal effects included, the required temperature enhancement is reduced by 100–150 K, while the required temperature bump up is almost the same. It is particularly necessary for reproducing the intensity enhancement at the center of the CaII 8542 Å line.

The computed thermal and non-thermal semi-empirical atmospheric models for the bright MF (No. 1) are given in Tables 2 and 3, respectively, where H is the height, M the column mass density, T the temperature, V_t the micro-velocity, $n_{\rm H}$ the hydrogen density and $n_{\rm e}$ the electron density.

4.2 Energetics of the Microflares

By using the semi-empirical atmospheric models of the MFs, the radiative energy can be estimated as follows: considering that the main heating regions are in the low-chromosphere, we use radiative losses to evaluate the radiative energy E_r:

$$E_r = \frac{D}{2} S_{\rm MF} \int_{h_1}^{h_2} R\, dh \ , \tag{4}$$

where D is the lifetime of the MF. The heating duration is assumed to be D/2. As we do not know the exact duration of the faint MF (No.3), we just take it to be 15 min. $S_{\rm MF}$ is the area of the MF which can be evaluated by the MF size listed in Table 1. In the formula h_1 and h_2 are the lower and the upper

Table 2 Thermal Semi-Empirical Model of the Bright Microflare (No.1)

No	H (km)	M (g cm^{-2})	T (K)	V_t (km s^{-1})	$n_{\rm H}$ (cm^{-3})	$n_{\rm e}$ (cm^{-3})
1	0.14993E+09	0.33730E-03	99500	0.98E+01	0.320E+12	0.386E+12
2	0.14988E+09	0.33735E-03	66600	0.90E+01	0.479E+12	0.576E+12
3	0.14950E+09	0.33800E-03	35300	0.80E+01	0.906E+12	0.109E+13
4	0.14601E+09	0.349610E-03	19082	0.66E+01	0.173E+13	0.190E+13
5	0.14468E+09	0.357780E-03	9802	0.65E+01	0.351E+13	0.318E+13
6	0.14335E+09	0.370450E-03	8661	0.58E+01	0.489E+13	0.111E+13
7	0.14145E+09	0.398287E-03	8109	0.53E+01	0.691E+13	0.580E+12
8	0.13474E+09	0.536779E-03	7703	0.47E+01	0.109E+14	0.378E+12
9	0.12564E+09	0.854175E-03	7286	0.38E+01	0.197E+14	0.281E+12
10	0.11496E+09	0.159967E-02	6719	0.31E+01	0.419E+14	0.188E+12
11	0.10533E+09	0.298241E-02	6352	0.25E+01	0.839E+14	0.169E+12
12	0.98035E+08	0.491555E-02	6035	0.20E+01	0.146E+15	0.157E+12
13	0.90259E+08	0.855122E-02	5811	0.14E+01	0.265E+15	0.176E+12
14	0.84615E+08	0.130232E-01	5570	0.92E+00	0.421E+15	0.170E+12
15	0.78772E+08	0.203976E-01	5456	0.78E+00	0.674E+15	0.199E+12
16	0.75859E+08	0.255100E-01	5621	0.75E+00	0.818E+15	0.294E+12
17	0.72698E+08	0.321819E-01	5888	0.73E+00	0.985E+15	0.514E+12
18	0.69321E+08	0.408100E-01	6148	0.70E+00	0.120E+16	0.919E+12
19	0.65838E+08	0.516600E-01	6329	0.64E+00	0.147E+16	0.150E+13
20	0.62235E+08	0.654600E-01	6478	0.62E+00	0.182E+16	0.240E+13
21	0.58606E+08	0.830200E-01	6355	0.60E+00	0.235E+16	0.230E+13
22	0.56845E+08	0.934497E-01	6193	0.59E+00	0.272E+16	0.187E+13
23	0.55151E+08	0.105130E+00	6000	0.58E+00	0.316E+16	0.147E+13
24	0.51916E+08	0.132730E+00	5701	0.56E+00	0.420E+16	0.111E+13
25	0.48885E+08	0.167330E+00	5401	0.54E+00	0.559E+16	0.950E+12
26	0.46729E+08	0.199110E+00	5100	0.52E+00	0.705E+16	0.939E+12
27	0.45375E+08	0.223085E+00	4996	0.52E+00	0.806E+16	0.101E+13
28	0.40875E+08	0.330423E+00	4815	0.66E+00	0.124E+17	0.137E+13
29	0.30811E+08	0.792164E+00	4983	0.76E+00	0.287E+17	0.314E+13
30	0.25838E+08	0.120233E+01	5127	0.90E+00	0.423E+17	0.482E+13
31	0.20883E+08	0.179833E+01	5328	0.11E+01	0.609E+17	0.754E+13
32	0.17191E+08	0.240056E+01	5521	0.12E+01	0.785E+17	0.110E+14
33	0.14722E+08	0.288863E+01	5761	0.14E+01	0.905E+17	0.160E+14
34	0.12747E+08	0.333218E+01	5940	0.14E+01	0.101E+18	0.227E+14
35	0.90502E+07	0.428258E+01	6392	0.16E+01	0.121E+18	0.572E+14
36	0.71305E+07	0.484757E+01	6740	0.17E+01	0.130E+18	0.112E+15
37	0.52083E+07	0.543782E+01	7326	0.17E+01	0.134E+18	0.303E+15
38	0.33066E+07	0.604445E+01	7886	0.18E+01	0.138E+18	0.693E+15
39	0.14140E+07	0.666258E+01	8481	0.18E+01	0.140E+18	0.148E+16
40	0.00000E+00	0.713133E+01	9030	0.18E+01	0.140E+18	0.272E+16

heights of the MF heating atmospheric region, respectively, and R is the non-LTE radiative losses in units of erg cm^{-3} s^{-1}, which was computed with the semi-empirical formula, given by Gan & Fang (1990):

$$R = n_{\rm H} n_e \alpha(H) f(T)\,, \tag{5}$$

where

$$\alpha(H) = \alpha_1(H) + \alpha_2(H)\,,$$
$$\log \alpha_1(H) = 2.75 \times 10^{-3} H - 5.445\,,$$
$$\alpha_2(H) = 2.3738 \times 10^{-4} e^{-H/163}\,,$$
$$f(T) = 1.547 \times 10^{-23} (T/10^4)^{3/2}\,.$$

The net radiative energy of the MF can be evaluated by

$$\Delta E = E_r - E_Q\ , \tag{6}$$

Table 3 Non-thermal Semi-empirical Model of the Bright Microflare (No.1)

No	H (km)	M (g cm^{-2})	T (K)	V_t (km s^{-1})	$n_{\rm H}$ (cm^{-3})	$n_{\rm e}$ (cm^{-3})
1	0.15043E+09	0.307300E–03	99500	0.98E+01	0.292E+12	0.351E+12
2	0.15037E+09	0.307349E–03	66600	0.90E+01	0.436E+12	0.525E+12
3	0.14996E+09	0.308001E–03	35300	0.80E+01	0.825E+12	0.992E+12
4	0.14735E+09	0.315212E–03	21350	0.69E+01	0.140E+13	0.153E+13
5	0.14510E+09	0.327780E–03	9802	0.65E+01	0.328E+13	0.242E+13
6	0.14367E+09	0.340450E–03	8861	0.58E+01	0.447E+13	0.102E+13
7	0.14151E+09	0.368287E–03	8109	0.53E+01	0.637E+13	0.525E+12
8	0.13448E+09	0.506779E–03	7553	0.47E+01	0.107E+14	0.330E+12
9	0.12531E+09	0.824175E–03	7116	0.38E+01	0.197E+14	0.257E+12
10	0.11460E+09	0.156967E–02	6619	0.31E+01	0.419E+14	0.198E+12
11	0.10508E+09	0.295241E–02	6202	0.25E+01	0.852E+14	0.173E+12
12	0.97853E+08	0.488555E–02	5975	0.20E+01	0.147E+15	0.188E+12
13	0.92791E+08	0.702300E–02	5800	0.16E+01	0.218E+15	0.202E+12
14	0.84582E+08	0.129932E–01	5500	0.92E+00	0.426E+15	0.255E+12
15	0.78836E+08	0.203676E–01	5356	0.78E+00	0.686E+15	0.401E+12
16	0.75974E+08	0.254800E–01	5501	0.75E+00	0.835E+15	0.619E+12
17	0.72896E+08	0.321519E–01	5728	0.73E+00	0.101E+16	0.131E+13
18	0.69601E+08	0.407800E–01	5984	0.70E+00	0.123E+16	0.765E+12
19	0.66193E+08	0.516300E–01	6209	0.64E+00	0.150E+16	0.184E+13
20	0.62643E+08	0.654300E–01	6459	0.62E+00	0.182E+16	0.254E+13
21	0.60818E+08	0.736919E–01	6489	0.61E+00	0.204E+16	0.290E+13
22	0.58068E+08	0.881900E–01	6419	0.59E+00	0.247E+16	0.288E+13
23	0.56616E+08	0.970995E–01	6309	0.58E+00	0.277E+16	0.251E+13
24	0.53748E+08	0.118130E+00	6078	0.57E+00	0.350E+16	0.191E+13
25	0.50531E+08	0.149036E+00	5669	0.55E+00	0.474E+16	0.120E+13
26	0.47542E+08	0.187775E+00	5350	0.53E+00	0.633E+16	0.103E+13
27	0.45422E+08	0.223055E+00	5096	0.52E+00	0.790E+16	0.105E+13
28	0.40884E+08	0.330393E+00	4825	0.66E+00	0.124E+17	0.138E+13
29	0.30811E+08	0.792134E+00	4983	0.76E+00	0.287E+17	0.315E+13
30	0.25838E+08	0.120230E+01	5127	0.90E+00	0.423E+17	0.482E+13
31	0.20883E+08	0.179830E+01	5328	0.11E+01	0.609E+17	0.755E+13
32	0.17192E+08	0.240053E+01	5521	0.12E+01	0.785E+17	0.110E+14
33	0.14722E+08	0.288860E+01	5761	0.14E+01	0.905E+17	0.160E+14
34	0.12747E+08	0.333215E+01	5940	0.14E+01	0.101E+18	0.227E+14
35	0.90503E+07	0.428255E+01	6392	0.16E+01	0.121E+18	0.572E+14
36	0.71305E+07	0.484754E+01	6740	0.17E+01	0.130E+18	0.112E+15
37	0.52084E+07	0.543779E+01	7326	0.17E+01	0.134E+18	0.303E+15
38	0.33066E+07	0.604442E+01	7886	0.18E+01	0.138E+18	0.693E+15
39	0.14140E+07	0.666255E+01	8481	0.18E+01	0.140E+18	0.148E+16
40	0.00000E+00	0.713130E+01	9030	0.18E+01	0.140E+18	0.272E+16

where $E_Q = \frac{D}{2} S_{\rm MF} \int R_Q dh$ is the total radiative losses of the quiet-Sun atmospheric model VALC. We take $\int R_Q dh = 4.6 \times 10^6$ erg cm^{-2} s^{-1} from Vernazza et al. (1981). In fact, our results indicate that E_Q is about one or two orders of magnitude smaller than E_r.

By use of the line-of-sight velocity measurement near the MFs, the lower limit of the kinetic energy can be estimated as

$$E_v = \frac{1}{2} 1.4 m_{\rm H} v_{\parallel}^2 f S_{\rm MF} \int_{h_3}^{h_4} n_{\rm H} dh \ , \tag{7}$$

where $n_{\rm H}$ is the hydrogen density in the heating region of the MF, f is the fraction of the mass that is involved in motion and we assume $f = 0.1$. The reasons are as follows: (1) The post-reconnection flows refer mainly to a pair of oppositely-oriented plasmoids (see e.g., Shibata et al. 1999); (2) in our observations mass motions are seen near, but not exactly at, the locations of the MFs, as indicated in Section 3.3. Thus, it seems that the heated plasma could not be fully ejected during the magnetic reconnection. The coefficient

Table 4 Parameters used to Estimate the Energy of the Two MFs

MF	h_1 (km)	h_2 (km)	h_3 (km)	h_4 (km)	$v_\parallel$ (km s^{-1})	ΔE (erg)	E_v (erg)
No.1	434	1440	434	862	2.0	3.8×10^{28}	1.5×10^{27}
No.3	399	1466	399	795	0.5	3.1×10^{27}	3.8×10^{25}

1.4 comes from the consideration of helium and other elements on the Sun, and corresponds to the mean density of the Sun (see Cox 1999). In Equation (7) h_3 and h_4 are, respectively, the lower and upper heights of the MF heating bump up area, determined by using the semi-empirical model of the MF. Due to the rapid decrease of the hydrogen density with height, the contribution of the higher layers is small. The measured line-of-sight velocity $v_\parallel$ is about 2 km s^{-1} for the bright MF (No.1), and and 0.5 km s^{-1} for the faint MF (No.3).

By use of the Equations (6) and (7), the energies of the two typical MFs can be estimated, as listed in Table 4. It can be seen that the total energy of the MFs is about 10^{27} to 4×10^{28} erg, and the energy of the brighter MF is larger than the fainter one.

5 DISCUSSION AND CONCLUSIONS

Using the THEMIS spectropolarimetric data, we have obtained the spectra of Hα, CaII 8542 Å, and FeI 6302 Å lines for five well-observed MFs. These spectral data were obtained simultaneously and with a high spatial resolution: this allows us make a good deduction of the the characteristics of the MFs.

The most obvious feature of the MF spectra is the emission at the centers of both the Hα and CaII 8542 Å lines. This implies that the heating of the Hα MF atmosphere occurs mainly in the chromosphere.

Three of the five MFs are located near the longitudinal magnetic polarity inversion lines (within 6 $''$) and all five are accompanied by mass motions (from 0.5 to several km s^{-1}). These facts imply that Hα MFs are probably caused by magnetic reconnection in the lower solar atmosphere. Two of the MFs are located in unipolar regions. However, this can not rule out the possibility of magnetic reconnection, because in the quasi-separatrix layers, where the the magnetic reconnection can occur (see Priest & Forbes 1999, and references therein), the line-of-sight component of the magnetic field can be unipolar.

Using non-LTE theory, we computed thermal semi-empirical models for one typical bright MF (No.1) and one faint MF (No.3). By including the non-thermal effects, we also obtained the non-thermal semi-empirical models. Our results indicate that the required extra heating in the chromosphere is about 1000–2200 K, and the higher value corresponds to the temperature bump up in the low-chromosphere, as clearly shown in Figures 5 and 6. It can account for the main spectral features of MFs, particularly the central emission of the CaII 8542 Å line. Moreover, if the non-thermal effects are included, the required extra heating can be reduced further. The reason is: If the non-thermal effect is included, then the particle beam will deposit their energy in the surrounding area, and contribute to the line emissions (e.g. Fang et al. 1993). This will reduce the contribution from the thermal component in the chromosphere, so the thermal temperature is reduced.

The semi-empirical models and the measured line-of-sight velocities near the MFs can be used to estimate both the radiative and kinetic energies. Our results indicate that the total energy is about 10^{27} to 4×10^{28} erg, and that the energy of the brighter MFs is larger than that of the fainter MFs.

It is worthwhile to compare MFs with Ellerman Bombs (EBs), which are small short-lived bright features observed best in the wings of chromospheric lines. Recently, we have analyzed some high-resolution spectra of EBs, and found that the temperature enhancement is about 600–1300 K, and is located mainly in the low-chromosphere and upper photosphere (Fang et al. 2006). By comparing the thermal semi-empirical models for EBs and MFs, it can be seen that the temperature bump up of EBs is deeper and lower than the MFs. Both of them could probably be caused by magnetic reconnection in the lower solar atmosphere, but the location of the magnetic reconnection is probably deeper for EBs than for MFs. This can be verified by some future numerical simulation.

As a summary, we give conclusions as follows:

1. The most obvious characteristic of the Hα MF spectra is an excess emission at the centers of both Hα and CaII 8542 Å lines.
2. Among the five well-observed MFs three are located near longitudinal polarity magnetic inversion lines, while two are located in unipolar regions. All the MFs are accompanied by mass motions. These imply that Hα MFs are probably produced by magnetic reconnection in the solar low-chromosphere.
3. For the first time both thermal and non-thermal semi-empirical atmospheric models for bright and faint MFs are given. Their common characteristic is the heating in the lower solar atmosphere with temperature enhancement of about 1000–2200 K. In particular, there is a temperature bump up in the low-chromosphere. If the non-thermal effects are included, the required temperature increase in the chromosphere will be reduced.
4. The radiative and kinetic energies for one bright and one faint MF have been estimated. The results indicate that the total energy of the MFs is 10^{27} – 4×10^{28} erg, and the energy of the brighter MFs is larger than that of the fainter one.

Acknowledgements We would like to give our sincere thanks to Dr. G. Ceppatelli, Dr. C. Briand and other staff at the Spanish Observatorio del Teide of the Institute de Astrofisica de Canarias for their enthusiastic help during C.F and Y.H.T's stay there. This work has been supported by NKBRSF No. 2006CB80632 and by the NSFC key project No. 10333040, as well as by the NSFC funds of Nos. 10073005, 19833040, 10173024 and 0403003.

References

Benz A. O., Grigis P. C., 2002, Solar Phys., 210, 431
Berghmans D., McKenzie D., Clette F., 2001, A&A, 369, 291
Chambe G., Hénoux J. -C., 1979, A&A, 80, 123
Chen P. F., Fang C., Ding M. D., 2001, Chin. J. Astron. Astrophys. (ChJAA), 1, 176
Cox A. N. (ed.), Allen's Astrophysical Quantities, Springer-Verlag, New York, 1999
Emslie A. G., 1978, ApJ, 224, 241
Emslie A. G., Noyes R. W., 1978, Solar Phys., 57, 373
Fang C., Hénoux J. C., Gan W. Q., 1993, A&A, 274, 917
Fang C., Ding M. D., Hénoux J.-C., Livingson W. C., 2001, Science in China, Ser.A, 44, 528
Fang C., Tang Y. H., Xu Z., Ding M. D., Chen P. F., 2006, ApJ, 643, 1325
Gan W. Q., Fang C., 1990, ApJ, 358, 328
Gary D. E., Zirin H., 1988, ApJ, 329, 991
Golub L., Kriger A. S., Silk J. K. et al., 1974, ApJ, 189, L93
Golub L., Krieger A. S., Harvey J. W. et al., 1977, Solar Phys., 53, 111
Hénoux J. -C., Fang C., Ding M. D., 1998, A&A, 182, 381
Krucker S., Christe S., Lin R. P. et al., 2002, Solar Phys., 210, 445
Lin R. P., Schwartz R. A., Kane S. R. et al., 1984, ApJ, 283, 421
Liu C., Qiu J., Gary D. E. et al., 2004, ApJ, 604, 442
Machado M. E., Avrett E. H., Vernazza J. E. et al., 1980, ApJ, 242, 336
Nindos A., Kundu M. R., White S. M., 1999, ApJ, 513, 983
Nitta N, 1997, ApJ, 491, 402
Parker E. N., 2001, Chin. J. Astron. Astrophys. (ChJAA), 1, 99
Porter J. G., Toomre J., Gebbie K. B., 1984, ApJ, 283, 879
Porter J. G., Moore R. L., Reichmann E. J. et al., 1987, ApJ, 323, 380
Priest E., Forbes T., 1999, in Magnetic Reconnection, Cambridge: Cambridge Uni. Press
Qiu J., Liu C., Gary D. E. et al., 2004, ApJ, 612, 530
Shibata K., 1999, ApSS, 264, 129
Shimizu T., Shine R. A., Title A. M. et al., 2002, ApJ, 574, 1074
Svestka Z., Solar Flares, 1976, Dordrecht: D.Reidel Publ. Co., Holland.
Tandberg-Hanssen E., Emslie A. G., The physics of solar flares, 1988, Cambridge: Cambridge University Press
Tang Y. H., Li Y. N., Fang C. et al., 2000, ApJ, 534, 482
Vernazza J. E., Avrett E. H., Loeser R., 1981, ApJS, 45, 635
Wang H., Chae J., Qiu J. et al., 1999, Solar Phys., 188, 365
White S. M., Kundu M. R., Shimizu T. et al., 1995, ApJ, 450, 435